Earth and Planetary Science
https://journals.nasspublishing.com/index.php/eps

ARTICLE

Joint Inversion of Gravity and Magnetic Data based on the Modified Structural Similarity Index for the Structural Consistency Constraint

Sheng Liu[1,2*], Yiju Tang[1], Fangchao Lu[1], Dali Sun[3], Bin Jia[1], Yuhao Ma[1]

1. Department of Safety Engineering, School of Municipal and Environmental Engineering, Henan University of Urban Construction, Pingdingshan, 467041, China
2. Institute of Geophysics, China Earthquake Administration, Beijing, 100080, China
3. The First Monitoring and Application Center, China Earthquake Administration, Tianjin, 300180, China

Abstract: Joint inversion is a crucial approach to mitigate the non-uniqueness problem in geophysical inversion. Nevertheless, existing joint inversion methods fall short of meeting the stringent requirements of high-precision exploration, necessitating the development of new techniques. In this paper, we introduce the Structural Similarity Index (SSIM) as a novel structural consistency constraint for the joint inversion of gravity and magnetic data. Compared with the results of cross-gradient inversion, our method demonstrates outstanding performance and stability. SSIM inversion not only introduces a new class of joint inversion with structural constraints but also enhances the consistency of inversion results in the distribution of physical attribute values. The structural constraints of SSIM inversion are more comprehensive and robust, significantly improving the reliability of the inversion. Both synthetic and real data applications demonstrate that the proposed method can effectively handle both synthetic and real data, yielding outstanding results.

Keywords: Joint inversion; Structural consistency constraints; Structural similarity index

1. Introduction

Geophysical data can be used to generate underground models through inversion methods, but the challenge lies in the existence of multiple solutions. To address this issue, prior information constraints and hybrid geophysical data for joint inversion have been proposed as effective strategies to reduce non-uniqueness [1–8].

Based on whether the recovered geophysical models are identical, geophysical joint inversion methods can be classified into two categories. The first category

*Corresponding Author:
Sheng Liu,
Department of Safety Engineering, School of Municipal and Environmental Engineering, Henan University of Urban Construction, Pingdingshan, 467041, China; Institute of Geophysics, China Earthquake Administration, Beijing, 100080, China;
Email: 20221100@hncj.edu.cn

Received: 24 April 2023; **Received in revised form:** 11 December 2023; **Accepted:** 16 April 2024; **Published:** 30 April 2024

Citation: Liu, S., Tang, Y., Lu, F., et al., 2024. Joint Inversion of Gravity and Magnetic Data based on the Modified Structural Similarity Index for the Structural Consistency Constraint. *Earth and Planetary Science*. 3(1): 44–54. DOI: https://doi.org/10.36956/eps.v3i1.849

DOI: https://doi.org/10.36956/eps.v3i1.849

involves jointly inverting multiple data sources for the identical petrophysical model, such as density models for gravity and gravity gradient data, velocity models for long-range and Rayleigh wave data, and resistivity models for DC and electromagnetic data [9–16]. Typically, this type of joint inversion method is relatively straightforward and can be easily implemented by incorporating data constraint items for other types of data into the objective function of separate inversion methods.

The second category, involving different geophysical data corresponding to different models, takes advantage of relationships between different petrophysical models. Joint inversion employs an empirical relationship between seismic velocity and gravity density models to reduce multiple solutions [17–18]. To reduce the ambiguity of inversion, the fuzzy C-means clustering algorithm can utilize the statistical relationship from the different petrophysical models [19,20]. Furthermore, numerous joint inversion methods are founded on cross-gradient constraint [21,22], correlation constraint [23–25] and Gramian constraint [26,27], which are extensively utilized for the joint inversion of diverse geophysical data.

The structural similarity index calculates structural similarity for different images comprehensively from three perspectives image brightness contrast function, contrast function and structural contrast function [28]. Generally, different physical property models obtained from different geophysical data within the same region are correlated. The petrophysical models can reckoned as different images, and the structural similarity index can serve as a constraint on structural consistency to constrain the physical property models. Additionally, the fractional form of the structural similarity index is converted to a denominator-subtracted-molecule format, which solves the analytical singularity in the denominator.

2. Methodology

2.1 Structural Similarity Index

The two physical parameters related to gravity and magnetic data are density $\boldsymbol{m}_1$ and susceptibility $\boldsymbol{m}_2$. According to the structural similarity quality evaluation algorithm [29], the structural similarity index between $\boldsymbol{m}_1$ and $\boldsymbol{m}_2$ is equation (1)

$$\mathrm{SSIM}(\boldsymbol{m}_1,\boldsymbol{m}_2)=\left[\mathrm{L}(\boldsymbol{m}_1,\boldsymbol{m}_2)\right]^{\alpha}\left[\mathrm{C}(\boldsymbol{m}_1,\boldsymbol{m}_2)\right]^{\beta}\left[\mathrm{S}(\boldsymbol{m}_1,\boldsymbol{m}_2)\right]^{\gamma} \tag{1}$$

where $\mathrm{L}(\boldsymbol{m}_1, \boldsymbol{m}_2)$ is brightness contrast function, $\mathrm{C}(\boldsymbol{m}_1, \boldsymbol{m}_2)$ is contrast function and $\mathrm{S}(\boldsymbol{m}_1, \boldsymbol{m}_2)$ is structure comparison function, α, β and γ are the parameters.

Thus, the processing methods of $\boldsymbol{x}=\boldsymbol{m}_1^2$ and $\boldsymbol{y}=\boldsymbol{m}_2^2$ are adopted, and the following structural similarity constraint can be obtained as equation (2) [30].

$$\Phi_{\mathrm{SSIM}}(\boldsymbol{x},\boldsymbol{y})=\left[\left(\mu_x^2+\mu_y^2\right)\left(\sigma_x^2+\sigma_y^2\right)\right]^2-\left(4\mu_x\mu_y\sigma_{xy}\right)^2 \tag{2}$$

where μ_x and μ_y are the mean values of $\boldsymbol{x}$ and $\boldsymbol{y}$, σ_x and σ_y are the variances of $\boldsymbol{x}$ and $\boldsymbol{y}$, σ_{xy} is the covariance of $\boldsymbol{x}$ and $\boldsymbol{y}$. In joint inversion, when the structures of the two physical property models are more similar, the value of structural similarity is smaller, which can be used as a new type of structural coupling constraint in joint inversion.

2.2 Objective Function of the Joint Inversion

Applying equation (2) to the objective function of a single inversion can obtain the objective function of SSIM inversion, such as equations (3) and (4).

$$\begin{aligned}\Phi_1=&\left\|\boldsymbol{d}_1-\boldsymbol{G}_1\boldsymbol{m}_1\right\|_2^2+\lambda_1\left\|\boldsymbol{w}_1\boldsymbol{m}_1\right\|_2^2\\&+\frac{1}{4}\gamma_1\left\{\left[\left(\mu_x^2+\mu_y^2\right)\left(\sigma_x^2+\sigma_y^2\right)\right]^2-\left(4\mu_x\mu_y\sigma_{xy}\right)^2\right\}\end{aligned} \tag{3}$$

and

$$\begin{aligned}\Phi_2=&\left\|\boldsymbol{d}_2-\boldsymbol{G}_2\boldsymbol{m}_2\right\|_2^2+\lambda_2\left\|\boldsymbol{w}_2\boldsymbol{m}_2\right\|_2^2\\&+\frac{1}{4}\gamma_2\left\{\left[\left(\mu_x^2+\mu_y^2\right)\left(\sigma_x^2+\sigma_y^2\right)\right]^2-\left(4\mu_x\mu_y\sigma_{xy}\right)^2\right\}\end{aligned} \tag{4}$$

where Φ_1 is the objective function of gravity anomaly data, $\boldsymbol{d}_1$ refers to the gravity data, $\boldsymbol{m}_1$ represents the recovered density model, $\boldsymbol{G}_1$ is the forward operator for gravity data, w_1 is the weighting matrix for the density model, λ_1 is the regularization parameter for gravity data, γ_1 is the weighting parameter for structural similarity in gravity, Φ_2 stands for the objective function of magnetic anomaly data, $\boldsymbol{d}_2$ refers to magnetic data, $\boldsymbol{m}_2$ represents the recovered susceptibility model, $\boldsymbol{G}_2$ is the forward operator for magnetic data, w_2 is the weighting matrix for the susceptibility model, λ_1 is the regularization parameter for magnetic data, and γ_2 is the weighting parameter for structural similarity in magnetic.

2.3 Model Update

To solve the objective function in the weighted pa-

rameter domain, set $\boldsymbol{m}_{1w} = \boldsymbol{w}_1\boldsymbol{m}_1$, $\boldsymbol{m}_{2w} = \boldsymbol{w}_2\boldsymbol{m}_2$, $\boldsymbol{G}_1^w = \boldsymbol{G}_1\boldsymbol{w}_1^{-1}$ and $\boldsymbol{G}_2^w = \boldsymbol{G}_2\boldsymbol{w}_2^{-1}$. The equations (3) and (4) can be transformed into the following form equation (5):

$$\Phi_1 = \left\|\boldsymbol{d}_1 - \boldsymbol{G}_1^w\boldsymbol{m}_{1w}\right\|_2^2 + \lambda_1\left\|\boldsymbol{m}_{1w}\right\|_2^2 + \frac{1}{4}\gamma_1\left\{\left[\left(\mu_x^2+\mu_y^2\right)\left(\sigma_x^2+\sigma_y^2\right)\right]^2 - \left(4\mu_x\mu_y\sigma_{xy}\right)^2\right\} \tag{5}$$

And equation (6)

$$\Phi_2 = \left\|\boldsymbol{d}_2 - \boldsymbol{G}_2^w\boldsymbol{m}_{2w}\right\|_2^2 + \lambda_2\left\|\boldsymbol{m}_{2w}\right\|_2^2 + \frac{1}{4}\gamma_2\left\{\left[\left(\mu_x^2+\mu_y^2\right)\left(\sigma_x^2+\sigma_y^2\right)\right]^2 - \left(4\mu_x\mu_y\sigma_{xy}\right)^2\right\} \tag{6}$$

For the convenience of calculation, the structural similarity constraint item does not change, but $\boldsymbol{m}_1$ and $\boldsymbol{m}_2$ are regarded as functions of $\boldsymbol{m}_{1w}$ and $\boldsymbol{m}_{2w}$, respectively. To simplify the derivative equation, we define μ_x and μ_y as constants whose values are determined by the values of the previous iteration. Thus, the derivatives of Φ_1 and Φ_2 with respect to $\boldsymbol{m}_{1w}$ and $\boldsymbol{m}_{2w}$ can be written as equation (7):

$$\frac{\partial\Phi_{\mathrm{SSIM}}}{\partial\boldsymbol{m}_{1w}} = \frac{\partial\Phi_{\mathrm{SSIM}}}{\partial\boldsymbol{x}}\frac{\partial\boldsymbol{x}}{\partial\boldsymbol{m}_1}\frac{\partial\boldsymbol{m}_1}{\partial\boldsymbol{m}_{1w}} = \begin{bmatrix}\left(\mu_x^2+\mu_y^2\right)^2\left(\boldsymbol{\sigma}_x^2+\boldsymbol{\sigma}_y^2\right)\mathrm{diag}(\boldsymbol{x}-\mu_x)\\ -8\left(\mu_x\mu_y\right)^2\boldsymbol{\sigma}_{\mathrm{xy}}\mathrm{diag}(\boldsymbol{y}-\mu_y)\end{bmatrix}\boldsymbol{w}_1^{-2}\boldsymbol{m}_{1w} \tag{7}$$

And equation (8):

$$\frac{\partial\Phi_{\mathrm{SSIM}}}{\partial\boldsymbol{m}_{2w}} = \frac{\partial\Phi_{\mathrm{SSIM}}}{\partial\mathbf{y}}\frac{\partial\mathbf{y}}{\partial\boldsymbol{m}_2}\frac{\partial\boldsymbol{m}_2}{\partial\boldsymbol{m}_{2w}} = \begin{bmatrix}\left(\mu_x^2+\mu_y^2\right)^2\left(\boldsymbol{\sigma}_x^2+\boldsymbol{\sigma}_y^2\right)\mathrm{diag}(\boldsymbol{y}-\mu_y)\\ -8\left(\mu_x\mu_y\right)^2\boldsymbol{\sigma}_{xy}\mathrm{diag}(\boldsymbol{x}-\mu_x)\end{bmatrix}\boldsymbol{w}_2^{-2}\boldsymbol{m}_{2w} \tag{8}$$

where diag[] indicates the transformation of a column vector into a diagonal matrix. The derivative of Φ_1 for $\boldsymbol{m}_{1w}$ can be written as equation (9):

$$\frac{\partial\Phi_1}{\partial\boldsymbol{m}_{1w}} = \left\{\begin{matrix}\boldsymbol{G}_{1W}^{\mathrm{T}}\boldsymbol{G}_{1W} + \lambda_1\boldsymbol{I}\\ +\frac{1}{4}\gamma_1\begin{bmatrix}\left(\mu_x^2+\mu_y^2\right)^2\left(\boldsymbol{\sigma}_x^2+\boldsymbol{\sigma}_y^2\right)\mathrm{diag}(\boldsymbol{x}-\mu_x)\\ -8\left(\mu_x\mu_y\right)^2\boldsymbol{\sigma}_{xy}\mathrm{diag}(\boldsymbol{y}-\mu_y)\end{bmatrix}\boldsymbol{w}_1^{-2}\end{matrix}\right\}\boldsymbol{m}_{1w} - \boldsymbol{G}_{1W}^{\mathrm{T}}\boldsymbol{d}_1 \tag{9}$$

Similarly, the derivative of Φ_2 with respect to $\boldsymbol{m}_{2w}$ can be expressed as equation (10):

$$\frac{\partial\Phi_2}{\partial\boldsymbol{m}_{2w}} = \left\{\begin{matrix}\boldsymbol{G}_{2W}^{\mathrm{T}}\boldsymbol{G}_{2W} + \lambda_2\boldsymbol{I}\\ +\frac{1}{4}\gamma_2\begin{bmatrix}\left(\mu_x^2+\mu_y^2\right)^2\left(\boldsymbol{\sigma}_x^2+\boldsymbol{\sigma}_y^2\right)\mathrm{diag}(\boldsymbol{y}-\mu_y)\\ -8\left(\mu_x\mu_y\right)^2\boldsymbol{\sigma}_{xy}\mathrm{diag}(\boldsymbol{x}-\mu_x)\end{bmatrix}\boldsymbol{w}_2^{-2}\end{matrix}\right\}\boldsymbol{m}_{2w} - \boldsymbol{G}_{2W}^{\mathrm{T}}\boldsymbol{d}_2 \tag{10}$$

Then, the conjugate gradient algorithm can be carried out, and the optimal $\boldsymbol{m}_1$ and $\boldsymbol{m}_2$ can finally be obtained.

3. Results and Validation

To verify the proposed joint inversion method, synthetic and actual data were used. In general, cross-gradient joint inversion is widely used for joint inversion. Therefore, this paper compares the SSIM inversion method with the cross-gradient inversion method to verify its effectiveness and advantages.

3.1 Model 1

The spatial distribution of Model 1 is shown in Figure 1a and 1b. The gravity and magnetic data calculated from this model are shown in Figure 1c and 1d. The gravity and magnetic data conform to a regular grid of 21 × 21 data points, for a total of 441 equidistant data points. During the inversion, there are 10 layers at a depth from 0 to 1000 m, and the mesh size is set to 100 × 100 × 100 m. At the same time, the workspace is divided into 20 × 20 × 10 grid cells.

Firstly, a separate inversion was performed using the reweighted conjugate gradient method, which was subsequently used for the other data sets. Figure 2a is the vertical density slice at x = 1000 m, and Figure 2b is the horizontal density slice at z = 400 m of the separate inversion results. Figure 2d shows the vertical magnetization slice at x = 1000 m, and Figure 2e shows the horizontal magnetization slice at z = 400 m of the separate inversion results. Comparing the results of gravity and magnetic inversion with the second model, the recovered density and magnetization roughly delineate the distribution range of anomalous bodies. But there is a big difference compared with the actual model. Figure 2c and 2f show the changes in the data misfits of separate inversions. The residuals of the separate inversion of gravity and magnetic data are 0.13 and 2.79, respectively.

Secondly, the cross-gradient joint inversion will be

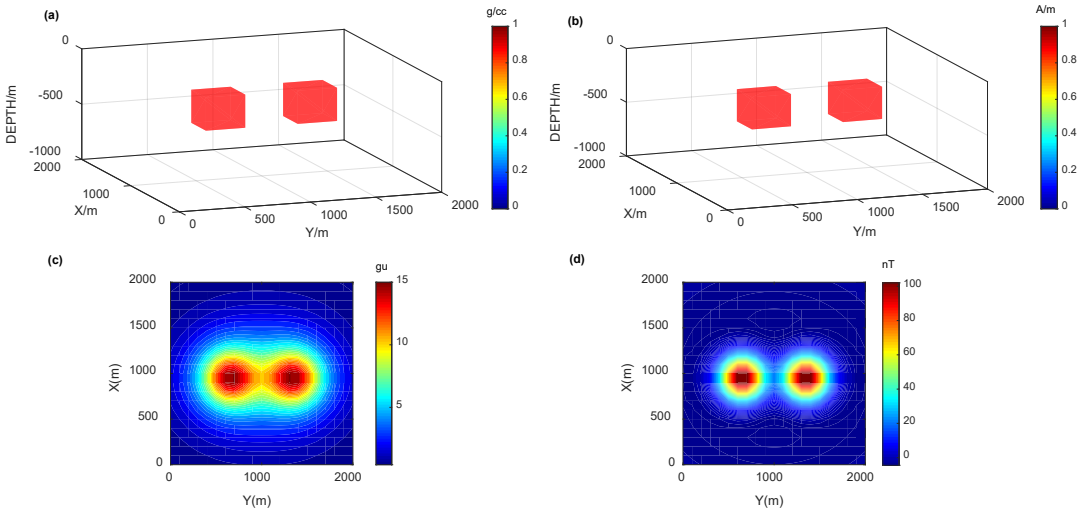

Figure 1. Spatial locations of the synthetic model 1 for density (**a**) and magnetization (**b**). The contour maps of forward gravity anomaly (**c**) and forward magnetic anomaly (**d**) of synthetic model 1.

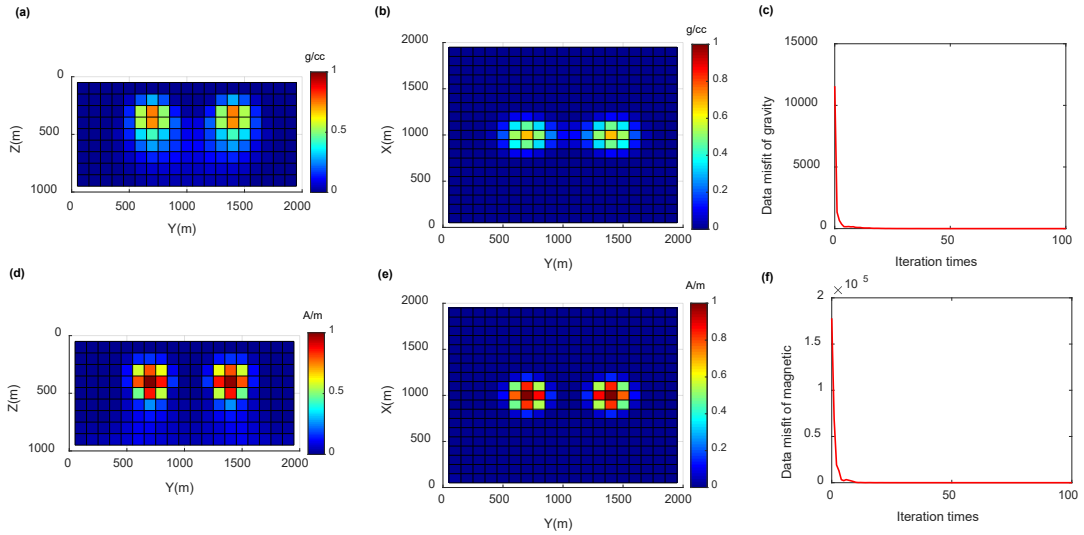

Figure 2. (**a**) and (**b**) are the slices of the separate inversion results of gravity data at x = 1000 m and z = 400 m, respectively. (**d**) and (**e**) are the slices of the separate inversion results of magnetic data at x = 1000 m and z = 400 m, respectively. (**c**) and (**f**) are the changes of the data misfits during the iterative process of separate inversion for gravity and magnetic data.

executed. Let the weighting factors of the cross-gradient constraint item be 3.0e7 and 1.0e6 for gravity and magnetic, and set the values of other parameters to be consistent with the individual inversions. Figure 3a is the vertical density slice at x = 1000 m, and Figure 3b is the horizontal density slice at z = 400 m of the cross-gradient inversion results. Figure 3d shows the vertical magnetization slice at x = 1000 m, and Figure 3e shows the horizontal magnetization slice at z = 400 m of the cross-gradient inversion results. Figure 3c and 3f show the changes in the data misfits of the cross-gradient inversions. The residuals of the cross-gradient inversion of gravity and magnetic data for model 2 are 2.22 and 2.61, respectively. Comparing the result of Figure 3 with the result of Figure 2, the density distribution obtained by the cross-gradient joint inversion has better vertical and horizontal distribution.

Then, let the weighted values of the SSIM constraint be 2.0e7 and 1.0e6 for gravity and magnetic inversion. Then, the SSIM inversion will be executed. Figure 4a is the vertical density slice at x = 1000 m, and Figure 4b is the horizontal density slice at z = 400 m of the SSIM inversion results. Figure 4d shows the vertical magnetization slice at x = 1000 m, and Figure 4e shows the

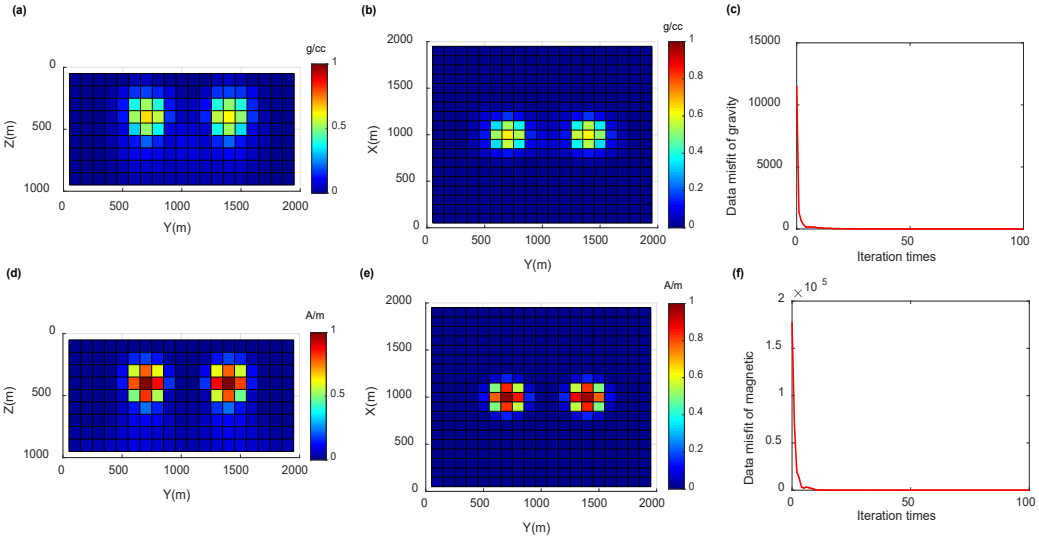

Figure 3. (**a**) and (**b**) represent the slices of the results obtained through cross-gradient inversion of gravity data at x = 1000 m and z = 400 m, respectively. (**d**) and (**e**) represent the slices of the results obtained through cross-gradient inversion of magnetic data at x = 1000 m and z = 400 m, respectively. (**c**) and (**f**) represent the changes in the data misfits resulting from joint inversion.

horizontal magnetization slice at z = 400 m of the SSIM inversion results. Figure 4c and 4f show the changes in the data misfits of SSIM inversion. The residuals for model 2 are 0.06 and 2.56, respectively. Comparing the results of Figures 4 and 3, it is found that the results of the SSIM inversion have been further improved. The vertical slice of density shown in Figure 4a has improved in spatial distribution, and the inverted density value has also become larger and more focused. Simultaneously, the horizontal slice value of the density shown in Figure 4b also becomes larger and more focused. Additionally, from the comparison of the above inversions for model 1, the final residual of the SSIM inversion is the smallest, which shows that the convergence is the best. Therefore, the SSIM inversion can not only proceed from the perspective of structural constraints but also from the size of the petrophysical models, which significantly improves the accuracy of the inversion results. Additionally, we find that the recovered density models improve greatly. Since the

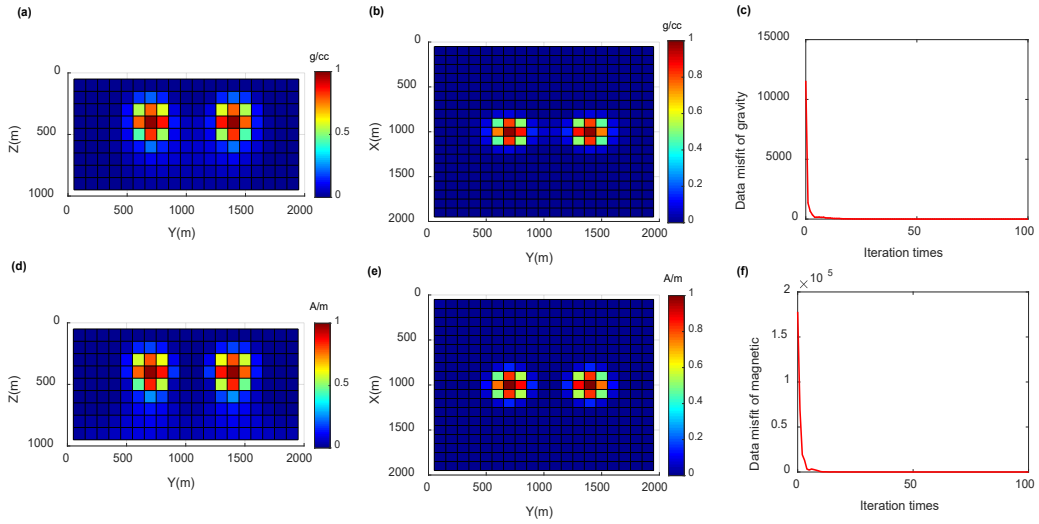

Figure 4. (**a**) and (**b**) are the cross-sections of the SSIM inversion results of gravity data at x = 1000 m and z = 400 m, respectively. (**d**) and (**e**) are the cross-sections of the SSIM inversion results of magnetic data at x = 1000 m and z = 400 m, respectively. (**c**) and (**f**) represent the misfit of data during the iterative process of SSIM inversion.

inverted magnetization intensity models are already very close to the actual models, their improvement is not very significant.

3.2 Model 2

A more intricate model was also utilized to verify the accuracy of the proposed approach. The spatial configuration of Model 2 is displayed in Figure 5a, 5b, 5d, and 5e. The gravitational and magnetic data computed from this model are shown in Figure 5c and 5f. Gravity and magnetic data adhere to a regular grid of 21 × 41 data points, totalling 861 equidistant data points. During the inversion process, there are 20 layers at a depth ranging from 0 to 1000 m, and the size of a cell is set to 100 × 100 × 100 m. Additionally, the work area is segmented into 40 × 20 × 20 grid cells.

Set the initial values of the density and magnetization models to 0.1. First, individual inversions will be performed. Figure 6a is a vertical density slice at x = 1000 m, and Figure 6b is a horizontal density slice at z = 1000 m of the separate inversion results. Figure 6d shows a vertical magnetization slice at x = 1000 m, and Figure 6e shows a horizontal magnetization slice at z = 1000 m of the separate inversion results. When comparing the results of gravity and magnetic inversions with model 2, the recovered density and magnetization roughly delineate the distribution range of anomalous bodies. However, there is a big difference compared

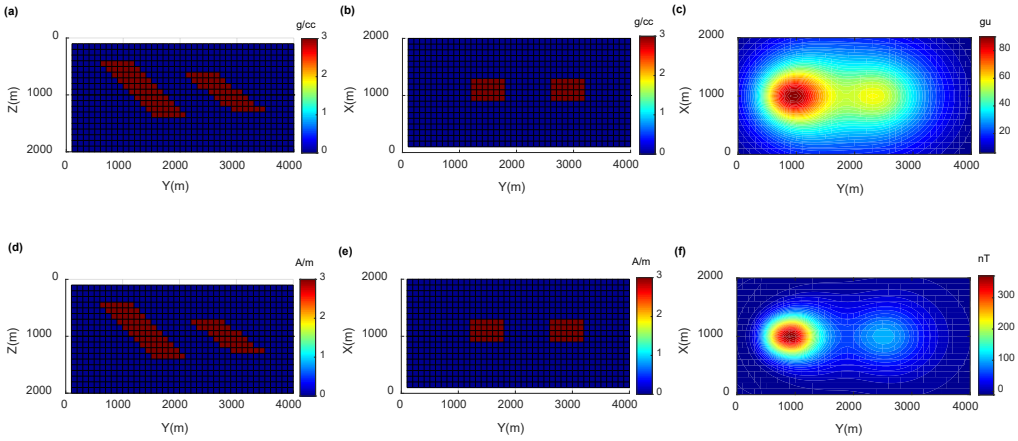

Figure 5. The cross-sections of the second density model at x = 1000 m (**a**) and z = 1000 m (**b**). (**c**) Gravity anomalies are calculated from the second density model. The cross-sections of the third magnetization model at x = 1000 m (**d**) and z = 1000 m (**e**). (**f**) The magnetic anomaly is calculated from the third magnetization model.

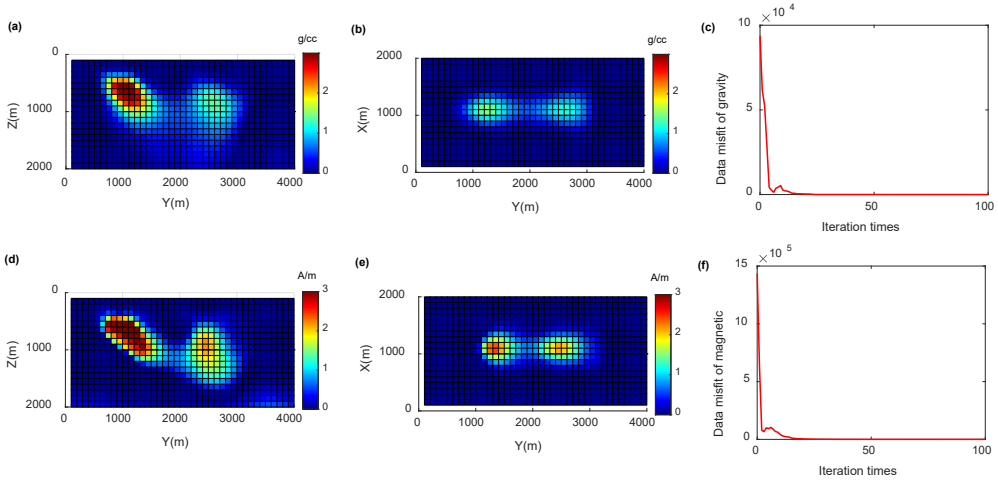

Figure 6. (**a**) and (**b**) are the slices of the separate inversion results of gravity data at x = 1000 m and z = 1000 m, respectively. (**d**) and (**e**) are the slices of the separate inversion results of magnetic data at x = 1000 m and z = 1000 m, respectively. (**c**) and (**f**) represent the changes in data misfits during the iterative process of separate inversion for gravity and magnetic data, respectively.

with the actual model. Figure 6c and 6f show the changes in the data misfits of separate inversions. The residuals of the separate inversion of gravity and magnetic data for model 3 are 3.90 and 89.54, respectively.

Secondly, the cross-gradient joint inversion will be executed. We set the weighting factor of the cross-gradient constraint item to 1.0e5, and align other parameters with the individual inversions of model 2. Figure 7a depicts a vertical density slice at x = 1000 m, while Figure 7b illustrates a horizontal density slice at z = 1000 m of the cross-gradient inversion results. Similarly, Figure 7d displays a vertical magnetization slice at x = 1000 m, and Figure 7e exhibits a horizontal magnetization slice at z = 1000 m of the cross-gradient inversion results. Figure 7c and 7f present the variations in data misfits during the cross-gradient inversions. Notably, the residuals from the cross-gradient inversion of gravity and magnetic data for model 3 amount to 15.44 and 136.11, respectively. Upon comparing Figure 7 with Figure 6, we observe that the density distribution achieved through cross-gradient joint inversion exhibits superior vertical and horizontal distribution, with a more concentrated density value. Hence, the results of the cross-gradient joint inversion have been significantly improved.

Finally, we set the parameter values to be identical to the corresponding values in the separate inversion. Additionally, we assign a weighted value of 0.1 to the SSIM inversion constraints. Subsequently, we proceed with the SSIM inversion for both gravity and magnetic data. Figure 8a is the vertical density slice at x = 1000 m, and Figure 8b is the horizontal density slice at z = 1000 m of the SSIM inversion results. Figure 8d shows the vertical magnetization slice at x = 1000 m, and Figure 8e shows the horizontal magnetization slice at z = 1000 m of the SSIM inversion results. Figure 8c and 8f show the changes in the data misfits of SSIM inversion. The residuals resulting from the SSIM inversion of gravity and magnetic data for model 2 are 4.82 and 80.41, respectively. Comparing the results of Figures 8 and 7, it is found that the results of the SSIM inversion have been further improved. The vertical slice of density shown in Figure 8a has improved in spatial distribution, and the inverted density value has also become larger and more focused. Simultaneously, the horizontal slice value of the density shown in Figure 8b also becomes larger and more focused. Additionally, from the comparison of the above inversions for model 2, the final residual of the SSIM inversion is the smallest, which shows that the convergence is the best. Comparing the two joint inversion results of this model, the SSIM inversion has certain advantages. As suggested by the findings of model 2, the utilization of SSIM inversion not only serves as a structural constraint but also enhances the consistency of the inversion results from the perspective of physical property values. The structure of the inversion result is not only more reasonable, but the physical property value is also more closely aligned with the actual model.

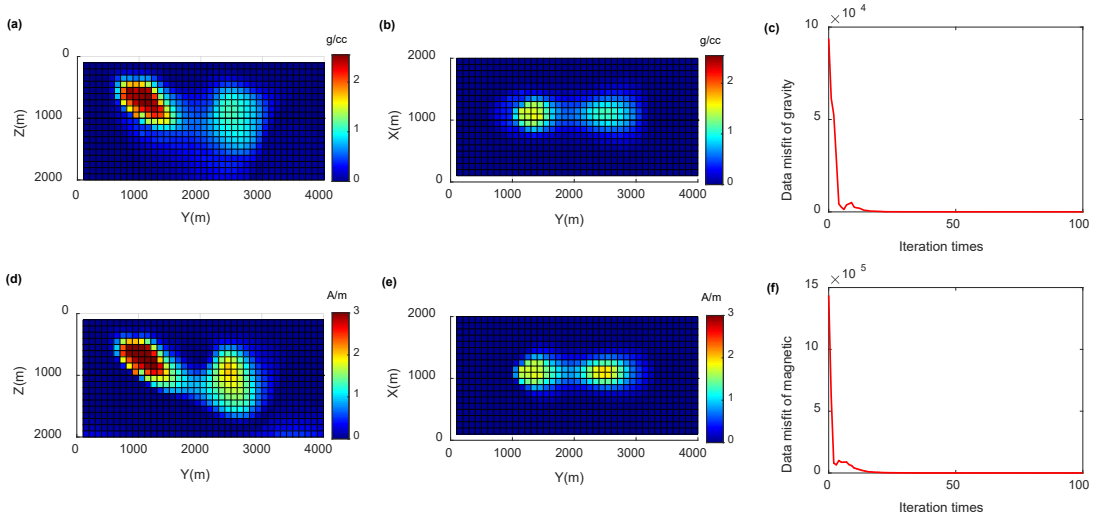

Figure 7. (**a**) and (**b**) are slices of the cross-gradient inversion results of gravity data at x = 1000 m and z = 1000 m, respectively. (**d**) and (**e**) represent slices of the cross-gradient inversion results of magnetic data at x = 1000 m and z = 1000 m, respectively. (**c**) and (**f**) depict the changes in data misfits during the iterative process of the cross-gradient inversion.

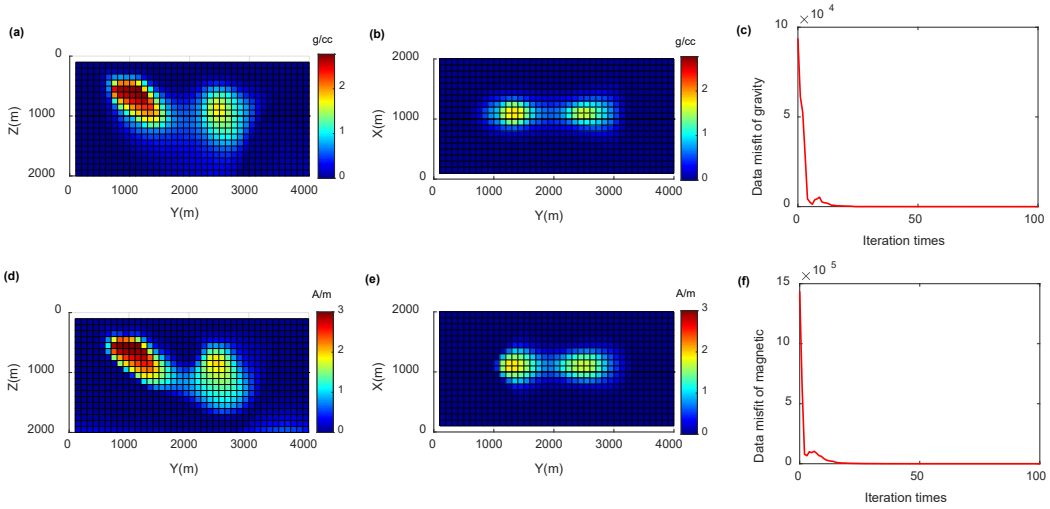

Figure 8. (**a**) and (**b**) are cross-sections of the SSIM inversion results for gravity data at x = 1000 m and z = 1000 m, respectively. (**d**) and (**e**) represent cross-sections of the SSIM inversion results for magnetic data at x = 1000 m and z = 1000 m, respectively. (**c**) and (**f**) depict the variations in data misfits during the iterative process of SSIM inversion.

3.3 Validation by the Field Data

This paper employs the SSIM inversion method to interpret gravity and magnetic data in the Pingbao lead-zinc-silver polymetallic mining area located in Hunan Province, China. Firstly, the regional gravity anomaly is removed from the measured anomaly, resulting in the residual gravity anomaly (Figure 9a). Similarly, after gridding the measured magnetic anomaly data, polarization processing is carried out to obtain the residual magnetic anomaly (Figure 9c). To perform a two-dimensional inversion, gravity and magnetic data extracted from an east-west trending profile (Figure 9b and 9d) are utilized in a programmed code of 2D SSIM inversion.

The observation line extends 6000 m, and the underground space of the inversion area is divided into 60 × 30 closely arranged rectangular units, each measuring 100 m × 100 m. Initially, gravity and magnetic data are inverted separately using a uniform half-space model with a density of 0.1 g/cc and a magnetization of 0.1 A/m. In the inversions, the model's physical properties are subject to interval constraints, with a density range set from

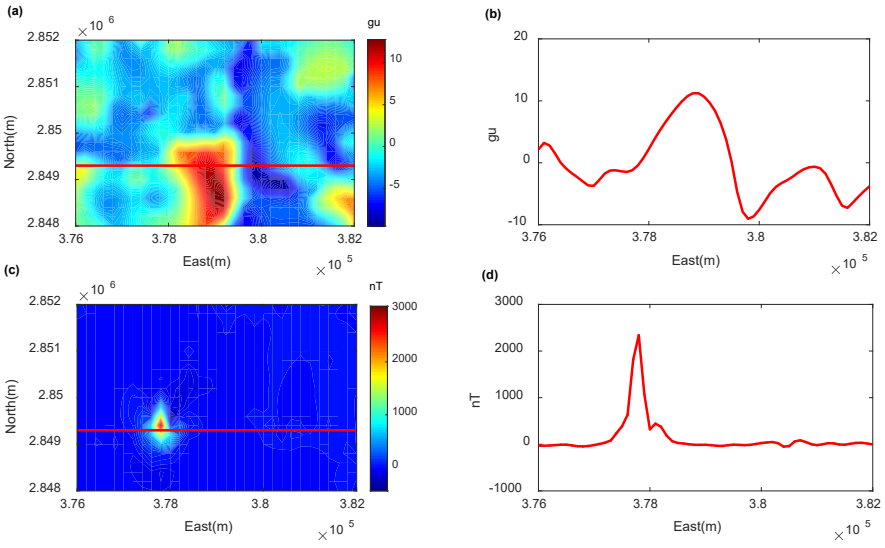

Figure 9. (**a**) Pingbao mining area in Hunan Province displays residual gravity anomaly data. (**b**) The gravity anomaly is observed along the red survey line depicted in (a). (**c**) Pingbao mining area in Hunan Province exhibits residual magnetic anomaly data. (**d**) The magnetic anomaly is observed along the red survey line shown in (c).

–3 g/cc to 3 g/cc and a magnetization range set from –3 A/m to 5 A/m. Additionally, the number of inversions is set to 200, and the fitting difference threshold is set to 1.0 × 102. Subsequently, separate inversions for real data are performed. The density slice of the inversion results is displayed in Figure 10a, and the inverted magnetization slice is shown in Figure 10c. Figure 10b and 10d exhibit the values of the data constraint items during the iterative process of separate inversions for gravity and magnetic data, respectively. The residuals of separate inversions for gravity and magnetic data on field data are 0.15 and 5.97, respectively. The separate inversions manage to distinguish between density and magnetization distributions. The density distribution corresponds well with gravity anomalies, exhibiting a pattern of high values in the center area and low values on both sides of the inverted area. Simultaneously, the anomalous magnetization distribution also displays a good correlation with magnetic data anomalies, showing high values in the center towards the west and low values on both sides of the inverted area. However, there exists a significant difference in the spatial distribution of the density model and magnetization model, resulting in poor consistency between them.

Subsequently, the SSIM inversion is performed using parameter values consistent with the separate inversions. Additionally, let γ_1 = 3.0e-6 and γ_2 = 2.0e-6. The density slice of the joint inversion result is shown in Figure 11a, and the magnetization slice is shown in Figure 11c. Figure 11b and 11d display the values of the data constraint items during the iterative process of SSIM inversion for gravity and magnetic data, respectively. Furthermore, the residuals of the SSIM inversion of gravity and magnetic data for field data are 0.13 and 17.17, respectively. The final residual of the joint inversion is approximately equal to the final residual of the separate inversion. The joint inversion can also distinguish between density and magnetization distributions. The density anomaly distribution corresponds well with gravity anomalies, exhibiting a pattern of high values in the center area and low values on both sides of the inverted area. Similarly, the anomalous magnetization distribution corresponds well with magnetic data anomalies, displaying a pattern of high values in the center towards the west and low values on both sides of the inverted area. Comparing Figure 11 with Figure 10, the former shows that the density distribution and the magnetization distribution are more focused, and the consistency of the structure distribution is also improved. Based on the petrophysical properties and logging data of the mining area, it is inferred that strong magnetic pyrite, magnetized skarn and lead-zinc-silver ore in this mining area are associated with skarn. The lead-zinc-silver polymetallic deposit's high density, coupled with the high magnetic properties of pyrite and magnetite skarn, allows for the retrieval of high density and magnetization distributions through joint inversion. This approach effectively delineates the regional location of polymetallic deposits and sharply defines the boundaries between the ore bodies and their surrounding rocks. However, it's worth noting that the congruence between the density model and magnetization intensity model resulting from the joint inversion is not particularly strong, potentially stemming from the inconsistent match between the underground model and actual data.

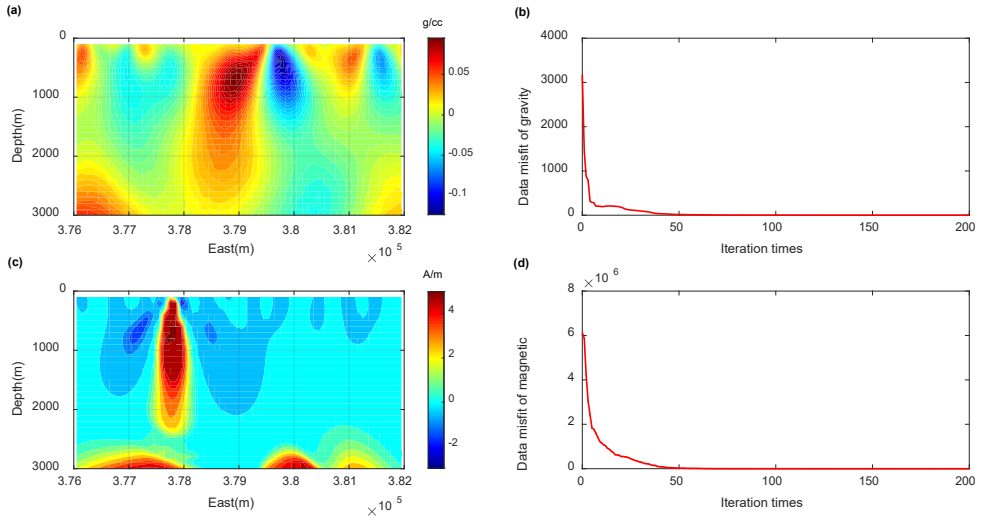

Figure 10. (**a**) The result of the separate inversion of gravity data. (**c**) The result of the separate inversion of magnetic data. (**b**) and (**d**) represent the changes in the data misfits during the iterations of the individual inversions.

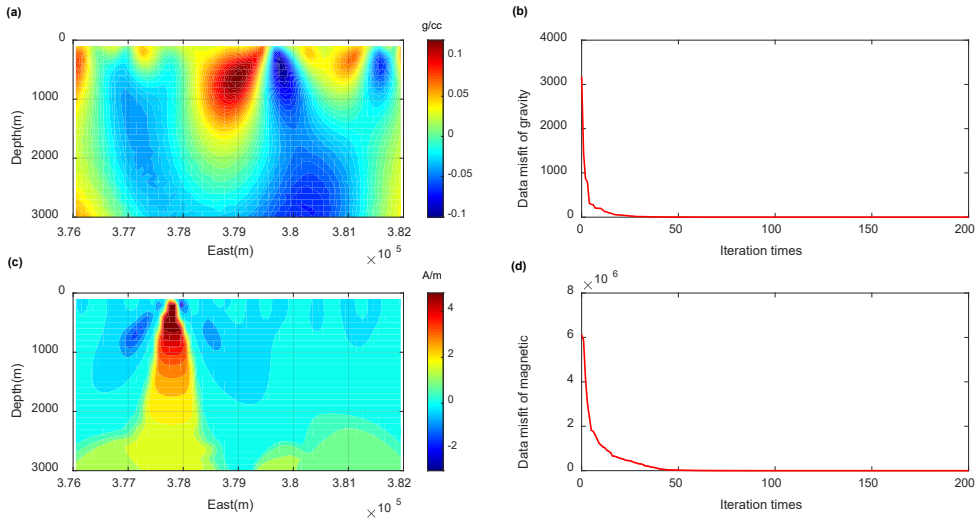

Figure 11. The joint inversion results yield both the density distribution (**a**) and magnetization distribution (**c**). The changes of data misfits during the iterative process of joint inversion for gravity and magnetic data are presented in (**b**) and (**d**), respectively.

4. Conclusions

We present a joint inversion method for gravity and magnetic data that incorporates a modified structural similarity index-based structural consistency constraint. This modified index utilizes a subtracted format instead of the traditional divided form, preventing analytical singularities and resulting in a more effective approach. Synthetic data experiments demonstrate the accuracy and effectiveness of our proposed approach, which outperforms separate inversions. When compared to cross-gradient inversion, SSIM inversion further enhances the inversion outcomes. Moreover, the application of SSIM inversion to actual data effectively identifies the regional location of the polymetallic deposit and delineates boundaries between ore bodies and surrounding rocks. This method not only introduces a new type of structurally constrained joint inversion but also promotes consistency across physical property values, reducing non-uniqueness during inversion. Our newly proposed approach demonstrates superior performance and high efficiency in joint inversion, offering promising prospects for geophysical inversion applications. We can find that the proposed method works well for the problem of joint inversion of homology, which is a very special joint inversion method, and its generalization needs further development.

Author Contributions

Sheng Liu carried out the analyses, interpreted the results and drafted the manuscript. Yiju Tang and Fangchao Lu guided the study and gave useful advice about the results. Dali Sun, Bin Jia, and Yuhao Ma took part in the design of the study. All authors read and approved the final manuscript.

Funding

This work was supported by the Henan Province Housing and Urban-Rural Development Science and Technology Program Project, Project No. (K-2319, K-2318, K-2310, HNJS-2022-K40), Henan Province Science and Technology Research Project, Project No. (242102320355, 242102321011), and State Key Laboratory Cultivation Base for Gas Geology and Gas Control (Henan Polytechnic University), Project No. (WS2023B08).

Data Availability Statement

Field data adopted in this paper are available on request from Sheng Liu.

Conflict of Interest

The authors disclosed no conflict of interest.

References

[1] Farquharson, C.G., Ash, M.R., Miller, H.G., 2008. Geologically constrained gravity inversion for the Voisey's Bay ovoid deposit. The Leading Edge. 27(1), 64–69.

[2] Lelièvre, P.G., Oldenburg, D.W., 2009. A comprehensive study of including structural orientation information in geophysical inversions. Geophysi-

cal Journal International. 178(2), 623–637.
[3] Afnimar, K.K., Nakagawa, K., 2002. Joint inversion of refraction and gravity data for the three-dimensional topography of a sediment-basement interface. Geophysical Journal International. 151(1), 243–254.
[4] Bosch, M., 1999. Lithologic tomography: From plural geophysical data to lithology estimation. Journal of Geophysical Research. 104(B1), 749–766.
[5] Bosch, M., Mc Gaughey, J., 2001. Joint inversion of gravity and magnetic data under lithologic constraints. The Leading Edge. 20(8), 877–881.
[6] Gallardo, L.A., Meju, M.A., 2003. Characterization of heterogeneous near-surface materials by joint 2D inversion of dc resistivity and seismic data. Geophysical Research Letters. 30(13).
[7] Lelièvre, P.G., Farquharson, C.G., Hurich, C.A., 2012. Joint inversion of seismic traveltimes and gravity data on unstructured grids with application to mineral exploration. Geophysics. 77(1), K1–K15.
[8] Moorkamp, M., Heincke, B., Jegen, M., et al., 2011. A framework for 3D joint inversion of MT, gravity and seismic refraction data. Geophysical Journal International. 184(1), 477–493.
[9] Guo, L., Meng, X., Shi, L., et al., 2009. 3D correlation imaging for gravity and gravity gradiometry data. Chinese Journal of Geophysics. 52(4), 1098–1106. (in Chinese).
[10] Chen, Z., Meng, X., Guo, L., et al., 2012. Three-dimensional fast forward modeling and the inversion strategy for large scale gravity and gravimetry data based on GPU. Chinese Journal of Geophysics. 55(12), 4069–4077. (in Chinese).
[11] Geng, M., Huang, D., Yang, Q., et al., 2014. 3D inversion of airborne gravity-gradiometry data using cokriging. Geophysics. 79(4), 37–47.
[12] Qin, P., Huang, D., Yuan, Y., et al., 2016. Integrated gravity and gravity gradient 3D inversion using the non-linear conjugate gradient. Journal of Applied Geophysics. 126, 52–73.
[13] Zhdanov, M.S., Lin, W., 2017. Adaptive multinary inversion of gravity and gravity gradiometry data. Geophysics. 82(6), G101–G114.
[14] Hou, Z., Huang, D., Wang, E., et al., 2019. 3D density inversion of gravity gradieometry data with amul tilevel hybrid parallel algorithm. Applied Geophysics. 16(2), 141–153.
[15] Fu, L., Liu, S., 2016. Joint inversion of first arrival P waves and Rayleigh waves based on cross-gradient constraint. Chinese Journal of Geophysics. 59(12), 4464–4472. (in Chinese).
[16] Vozoff, K., Jupp, D.L.B., 1975. Joint inversion of geophysical data. Geophysical Journal International. 42(3), 977–991.
[17] Gardner, G.H.F., Gardner, L.W., Gregory, A.R., 1974. Formation velocity and density-the diagnostic basics for stratigraphic traps. Geophysics. 39(6), 770–780.
[18] Lines, L.R., Schultz, A.K., Treitel, S., 1988. Cooperative inversion of geophysical data. Geophysics. 53(1), 8–20.
[19] Sun, J., Li, Y., 2015. Multidomain petrophysically constrained inversion and geology differentiation using guided fuzzy c-means clustering. Geophysics. 80(4), ID1–ID18.
[20] Sun, J., Li, Y., 2016. Joint inversion of multiple geophysical data using guided fuzzy c-means clustering. Geophysics. 81(3), ID37–ID57.
[21] Haber, E., Oldenburg, D, 1997. Joint inversion a structural approach. Inverse Problems. 13, 63–77.
[22] Fregoso, E., Gallardo, L.A., 2009. Cross-gradients joint 3D inversion with applications to gravity and magnetic data. Geophysics. 74(4), L31–L42.
[23] Oldenburg, D.W., Li, Y., 1999. Estimating depth of investigation in dc resistivity and IP surveys. Geophysics. 64(2), 403–416.
[24] Yin, C., Sun, S., Gao, X., et al., 2018. 3D joint inversion of magnetotelluric and gravity data based on local correlation constraints. Chinese Journal of Geophysics. 61(1), 358–367. (in Chinese).
[25] Shi, B., Yu, P., Zhao, C., et al., 2018. Linear correlation constrained joint inversion using squared cosine similarity of regional residual model vectors. Geophysical Journal International. 215(2), 1291–1307.
[26] Zhdanov, M.S., Gribenko, A., Wilson, G., 2012. Generalized joint inversion of multimodal geophysical data using Gramian constraints. Geophysical Research Letters. 39(9).
[27] Lin, W., Zhdanov, M.S., 2018. Joint multinary inversion of gravity and magnetic data using Gramian constraints. Geophysical Journal International. 215(3), 1540–1557.
[28] Zhou, W., Bovik, A.C., Sheikh, H.R., et al., 2004. Image quality assessment: From error visibility to structural similarity. IEEE Transactions on Image Processing. 13(4), 600–612.
[29] Zhou, W., Bovik, A.C., 2009. Mean squared error: Love it or leave it? IEEE Signal Processing Magazine. 26(1), 98–117.
[30] Liu, S., Wan, X., Jin, S., et al., 2023. Joint inversion of gravity and vertical gradient data based on modified structural similarity index for the structural and petrophysical consistency constraint. Geodesy and Geodynamics. 14(5), 485–499.